Scientific Contributions Oil & Gas, Vol. 48. No. 4, December: 35 - 49

SCIENTIFIC CONTRIBUTIONS OIL AND GAS

Testing Center for Oil and Gas
LEMIGAS

Journal Homepage:http://www.journal.lemigas.esdm.go.id
ISSN: 2089-3361, e-ISSN: 2541-0520

# Porosity Estimation in A Natural $CO_2$-Water Reservoir Using Integrated Density-Resistivity Log Approach

Pahala Dominicus Sinurat[1], Hari Sasongko[2], and Nabil Visi Samawi[1]

[1]Institut Teknologi Bandung
Ganesha Street No.10, Lebak Siliwangi, Coblong, Bandung City, West Java 40132, Indonesia.

[2]Infosys Consulting
818 Town & Country Blvd Suite 600, Houston, TX 77024, USA.

Corresponding author: Pahala Dominicus Sinurat (sinurat@itb.ac.id)

Manuscript received: October 07th, 2025; Revised: October 23th, 2025
Approved: October 29th, 2025; Available online: December 05th, 2025; Published: December 05th, 2025.

**ABSTRACT** - Natural $CO_2$ reservoirs represent important analogues for Carbon Capture and Storage (CCS) and Carbon Capture, Utilization, and Storage (CCUS), as they provide direct evidence of long-term $CO_2$ retention and trapping mechanisms. This study assesses porosity in a natural carbonate $CO_2$ reservoir using an integrated density–resistivity log approach. Conventional porosity logs, such as density, neutron, and sonic, often overestimate porosity in carbonate systems due to their limited sensitivity to pore connectivity. To overcome this limitation, density log-derived total porosity was integrated with resistivity-derived effective porosity, allowing for the differentiation between connected and isolated pore systems. Fluid density estimations, including supercritical $CO_2$ and brine, were computed and validated against standard references to ensure accuracy. The results show that density-only porosity overestimates values by up to 10% in dolomitic intervals, whereas the integrated method provides estimates that are more consistent with core measurements. Isolated porosity, averaging 2% in the upper dolomite and 1.5% in the lower dolomite, was identified as a non-contributing pore volume for injectivity, although it remains relevant for storage capacity. These findings underscore the importance of integrated log interpretation for precise reservoir characterization and offer new insights into evaluating natural $CO_2$ reservoirs for long-term geological storage.

**Keywords**: $CO_2$ reservoir, carbonate reservoir, density–resistivity integration, well log.



**How to cite this article:**

Pahala Dominicus Sinurat, Hari Sasongko, and Nabil Visi Samawi, 2025, Porosity Estimation in A Natural $CO_2$-Water Reservoir Using Integrated Density-Resistivity Log Approach, Scientific Contributions Oil and Gas, 48 (4) pp. 35-49. DOI org/10.29017/scog.v48i4.1887.

## INTRODUCTION

Although the current global transition toward renewable energy marks a positive trajectory in advancing sustainable energy systems, fossil fuels are still projected to account for approximately 58% of total energy demand in 2050 (IEA 2024).

Abrupt discontinuation of investment in the oil and gas sector could lead to substantial disruptions in global economic stability (Exxon 2024). In response, many countries have announced long-term strategies to achieve net-zero greenhouse gas (GHG) emissions by 2050 (IPCC 2025). Within this context, Carbon Capture and Storage (CCS) and Carbon Capture, Utilization, and Storage (CCUS) have emerged as crucial technologies for mitigating $CO_2$ emissions while maintaining a sustainable energy supply (Bachu 2008; Krevor et al., 2015). Natural $CO_2$ reservoirs, which have stored carbon dioxide safely over geological timescales, provide important analogues for CCS projects. They provide direct insights into trapping mechanisms and long-term storage security that are challenging to replicate in short-term pilot projects. Miocic et al. (2013) analyzed a dataset of 49 natural $CO_2$ reservoirs worldwide and confirmed their significance in understanding leakage risk and reservoir performance. Such studies underscore the need for a deeper understanding of natural $CO_2$ reservoirs, serving as a critical reference for sequestration projects (Gilfillan et al., 2009). A critical factor in $CO_2$ storage is its supercritical condition, which is reached at pressures above 12.4 MPa and temperatures above 180 °F, where $CO_2$ exhibits a liquid-like density and a gas-like viscosity. The density of $CO_2$ under these conditions governs both storage capacity and flow dynamics in porous media. Several correlations, such as the Span & Wagner (1996) equation of state, as well as those by Liang et al. (2014) and Wang et al. (2015), have been developed to predict $CO_2$ density under reservoir conditions. Incorporating this property into log interpretation workflows enhances the reliability of porosity estimation in supercritical $CO_2$ reservoirs.

In carbonate reservoirs, however, conventional porosity logs (density, neutron, and sonic) often face limitations due to complex pore systems. Density logs tend to measure total porosity, including isolated pores, whereas resistivity logs derived from Archie's equation are more sensitive to effective porosity, reflecting fluid-connected pores. Sonic logs, although more precise for effective porosity, were not used in this study due to inconsistencies with other logs. Neutron logs were also excluded, as their response under supercritical $CO_2$ conditions does not reliably represent hydrogen content. As a result, using density logs alone can lead to overestimation of effective porosity (Tiab & Donaldson 2015).

To address these limitations, this study proposes an integrated porosity estimation method that combines density and resistivity logs to enhance accuracy. This approach enables differentiation between total and effective porosity, as well as quantification of isolated pore systems. By comparing log-derived porosity with core measurements, this method provides a more accurate basis for evaluating natural $CO_2$ reservoirs as long-term storage sites. It contributes to improving reservoir characterization for CCS/ CCUS applications.

## METHODOLOGY

Clay typing was conducted to evaluate the potential influence of clay minerals on log responses and porosity interpretation. Figure 2 presents the clay typing chart based on the Schlumberger Lith-2 cross-plot, which uses thorium and potassium content from spectral gamma ray measurements. The plot shows that the data do not correspond to any distinct clay type such as kaolinite, illite, smectite, or mixed-layer clays. This indicates the absence of a pure shale zone within the studied interval.

Since thorium and potassium are reliable proxies for differentiating clay minerals, their low concentrations suggest that clay content in this reservoir is minimal. For porosity analysis, the clay effect can therefore be considered negligible. This finding is consistent with observations in carbonate reservoirs, where clay minerals typically have a lesser impact on porosity compared to siliciclastic formations (Asquith & Krygowski, 2004; Rider & Kennedy 2011). Consequently, no shale correction was applied to the log data in subsequent porosity computations.

### Data preparation

The dataset used in this study consisted of gamma ray, density, neutron, and resistivity logs, complemented by core porosity data. Pre-

processing included quality control, environmental correction, and core–log depth shifting (Figure 3). This step is essential to minimize depth mismatch, which can otherwise cause significant errors in porosity validation (Doveton 2014).

Clay typing was conducted using spectral gamma ray cross-plots of thorium versus potassium (Figure 2). The absence of clustering in typical clay zones indicated negligible shale content. This result justifies the assumption that clay effects on porosity estimation are minor in this carbonate reservoir (Asquith & Krygowski 2004).

**Fluid density computation**

**Supercritical $CO_2$ density**

The supercritical $CO_2$ density is calculated based on Liang's correlation (2014) as follows:

$$\rho = A_o + A_1\, p + A_2\, p^2 + A_3\, p^3 + A_4\, p^4 \quad (1)$$

where

$$A_i = b_{i0} + b_{i1} + b_{i2}T^2 + b_{i3}T^3 + b_{i4}T^4 \quad (i = 0,1,2,3,4) \quad (2)$$

The coefficients for pressures greater than 3,000 psia. At reservoir conditions (3,602 psi and 132 ° F), the estimated $CO_2$ density is 0.8056 g/cc. These results were compared against the NIST database (Span & Wagner 1996), which is considered the benchmark equation of state.

The coefficients used in this study are summarized in Table 1, which provides the polynomial constants b0–b4 as functions of temperature. These constants enable the correlation to predict $CO_2$ density reliably for pressures above 3,000 psia. As shown in Table 1, the correlation incorporates temperature-dependent terms up to the fourth order, enabling accurate density predictions under reservoir conditions. At 3,602 psi and 132 ° F, the estimated $CO_2$ density was 0.8056 g/cc, which is consistent with values from the NIST database (Span & Wagner 1996). This validates the applicability of Liang's correlation for the conditions analyzed in this study.

**Brine density**

The water density is calculated based on McCain's correlation. The first step is to calculate the brine formation volume factor:

$$B_w = \frac{1 + \Delta V_{wp}}{1 + \Delta V_{wT}} \quad (3)$$

where

$$\Delta V_{wT} = -1.0001\,(10^{-2}) + 1.33391\,(10^{-4}) + 5.50654\,(10^{-7})T^2 \quad (4)$$

and

$$\Delta V_{wp} = -1.95301\,(10^{-9})pT - 1.72834\,(10^{-13})p^2T - 3.58922\,(10^{-7})p - 2.25341p^2 \quad (5)$$

Then, we use correlation to estimate the brine density based on the total dissolved solid weight percent.

$$\rho_{w_{@\,surface}} = 62.368 + 0.438603\,S + 1.60074\,(10^{-3})\,S^2 \quad (6)$$

Finally, the brine density as a reservoir condition is calculated based on the water formation volume factor at a particular depth and corresponding pressure and temperature:

$$\rho_w = \frac{\rho_{w_{@\,surface}}}{B_w} \quad (7)$$

Table 1. Polynomial coefficients ($b_0$–$b_4$) in liang's $CO_2$ density correlation

| | $b_{i0}$ | $b_{i1}$ | $b_{i2}$ | $b_{i3}$ | $b_{i4}$ |
|---|---|---|---|---|---|
| i = 0 | 6.897382693936E+02 | 2.730479206931E+00 | -2.254102364542E-02 | -4.651196146917E-03 | 3.439702234956E-05 |
| i = 1 | 2.213692462613E-01 | -6.547268255814E-03 | 5.982258882656E-05 | 2.274997412526E-06 | -1.888361337660E-08 |
| i = 2 | -5.118724890479E-05 | 2.019697017603E-06 | -2.311332097185E-08 | -4.079557404679E-10 | 3.893599641874E-12 |
| i = 3 | 5.517971126745E-09 | -2.415814703211E-10 | 3.121603486524E-12 | 3.171271084870E-14 | -3.560785550401E-16 |
| i = 4 | -2.184152941323E-13 | 1.010703706059E-14 | -1.406620681883E-16 | -8.957731136447E-19 | 1.215810469539E-20 |

The same equation is used for mud filtrate density calculation in the invaded zone. To compare the results, we use the National Institute of Standards and Technology (NIST) database.

**Porosity computation**

The same equation is used for mud filtrate density calculation in the invaded zone. To compare the results, we use the National Institute of Standards and Technology (NIST) database.

As shown in Figure 6, at a lower pressure of around 3,000 psi, the computation results yield slightly higher values than those from NIST. The NIST uses Span & Wagner correlation (1996). We tried a new correlation from Wang et al. (2015); however, it gives unrealistic values.

The density log reads electron density instead of the bulk density. For every element and compound molecule, a conversion should be made from bulk density to electron density, and then eventually to the tool reading. The atomic or molecular number and weight relate to the bulk and electron density.

For $CO_2$, the estimated density at 3,602 psi and 132 °F is 0.8056 g/cc (using Liang's method, as implemented in the program). The electron density The electron density related to bulk density is:

$$\rho_e = \rho_b \frac{2\,Z}{MW} = 0.8056\,\frac{2\,(6+2\times 8)}{(12.011+2\times 16)} = 0.8054 \tag{8}$$

The tool reading is calibrated based on a reference lithology. For pure, fully water-saturated limestone:

$$\rho_a = 1.0704\,\rho_e - 0.1883 \tag{9}$$

Therefore, in pure supercritical $CO_2$, the density tool should read:

$$\rho_a = 1.0704\,\times 0.8054 - 0.1883 = 0.6741 \tag{10}$$

In the computation, the initial porosity estimation is calculated based on:

$$\phi = \sqrt{\frac{{\phi_D}^2 + {\phi_N}^2}{2}} \tag{11}$$

However, since the neutron log does not correspond to hydrogen content, the neutron log data is not being used. In this work, we estimate the effective porosity by integrating the resistivity log using Archie's equation and the density log.

Considering the mud invasion phenomenon, the resistivity log reading in the uninvaded zone should be affected by the initial formation fluid (formation water and supercritical $CO_2$). The deepest resistivity reading is expected to be in the uninvaded zone. The mnemonics for resistivity curves are R30O, R40O, R60O, R85O, and RTAO. We do not recognize this mnemonics, but we think it is an array induction log. The geothermal gradient is calculated to estimate the temperature at every depth. For Archie's equation, the values of a, m, and n are 1, 1.99, and 2, respectively.

The formation water saturation is calculated at every depth by using Arp's equation. The Arp's equation estimates resistivity variations based on temperature and salt concentration:

$$R_w = \left[0.0123 + \frac{3647.5}{\left(NaCl_{ppm}\right)^{0.955}}\right]\left[\frac{81.77}{T+6.77}\right] \tag{12}$$

The following equation calculates mud filtrate resistivity at every depth:

$$R_{mf_{@Depth}} = R_{mf_{@Surface}}\,\frac{T_{@Surface}+6.77}{T_{@Depth}+6.77} \tag{13}$$

The algorithm for porosity computation is shown in Figures 1 and 2. Figure 1 represents porosity computation in the uninvaded zone, while Figure 2 represents the invaded zone.

Figure 8 illustrates the difference in porosity estimation between the density log alone (total porosity) and the integrated method presented in this work. It is observed that the difference in the interest zones (dolomite) is about 10%.

To validate log-derived porosity, core data after shifting is used. Figure 9 shows that the log-derived porosity matches most of the lower parts of dolomites. Some cores with very low porosity (less than 5% at intervals 8,080–8,130 ft) require further verification. Overall, the porosity between the core and log-derived samples shows a good correlation.

The porosity estimation result will be used for permeability prediction in the following progress report.

In carbonate reservoirs, it is common to have multiple types of porosity, such as interparticle, vugs, and fractures. Dissolved particles form vugs (smaller size) and caverns (bigger size). The supercritical $CO_2$ and rock interactions force clay mineral splitting and mineral dissolution (cementing, filling, and calcium carbonate aggregate itself). The final product of the chemical reaction is the precipitation of minerals. The precipitation could change small connected pores into an isolated pore system.

Figure 10 shows the estimated isolated porosity based on the difference between effective porosity (calculated from integration resistivity and density) and total porosity (density log alone). Figure 9 illustrates that the dolomite sections contain more isolated pores. The average of isolated pores is about 2% in the upper dolomite section and 1.5% in the lower dolomite section.

Porosity is calculated using Archie's equation as follows:

$$\phi = \left(\frac{a}{S_w{}^n}\frac{R_w}{R_t}\right)^{\frac{1}{m}} \quad (14)$$

Then the fluid density is calculated using:

$$\rho_{f_a} = S_w \rho_{w_a} + S_{sCO_2}\rho_{sCO_{2_a}} \quad (15)$$

**Research workflow**

To address mud-filtrate invasion, porosity was computed separately for uninvaded and invaded zones. The iterative algorithms are summarized in Figures 1 and 2.

Figure 1: Porosity computation in the uninvaded zone, using deep resistivity data less affected by invasion.

Figure 2: Porosity computation in the invaded zone, incorporating mud-filtrate resistivity into Archie's formulation.

This dual approach ensures robust estimation of porosity across different invasion conditions.

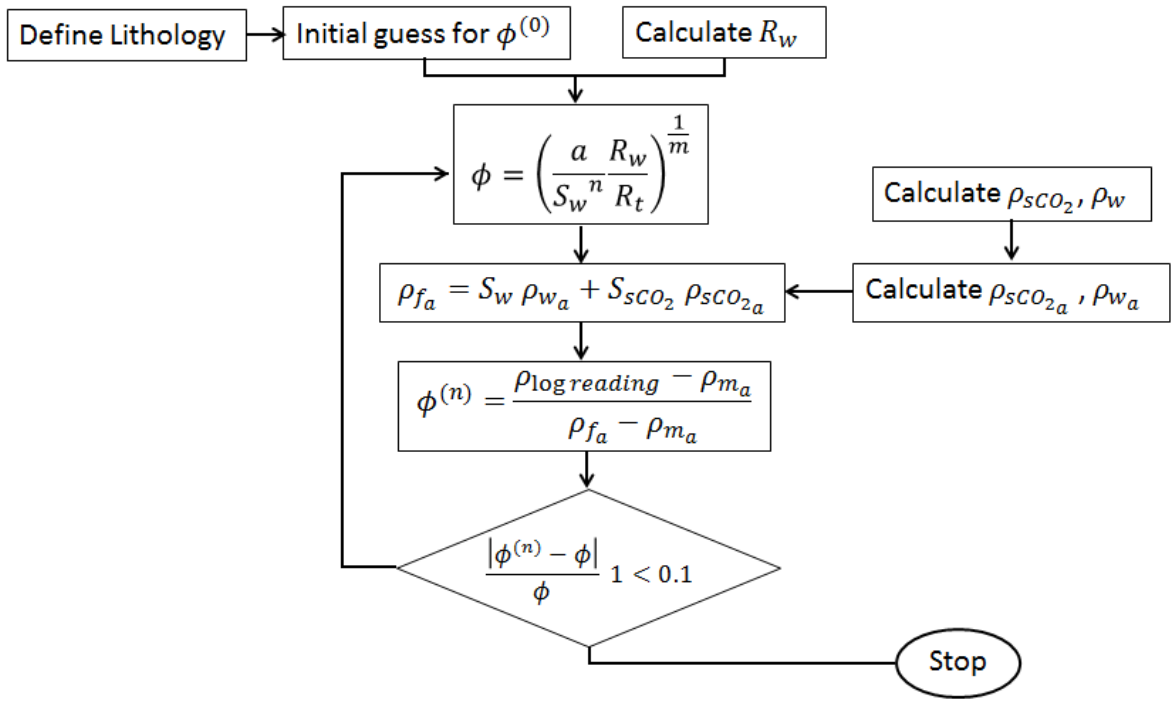


Figure 1. Porosity computation for uninvaded zone $R_t$

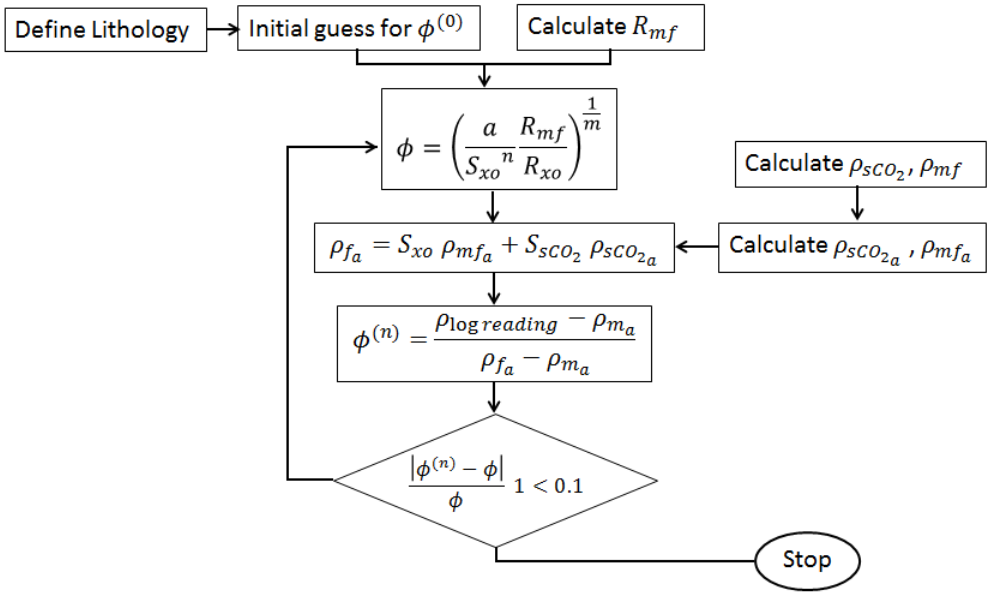


Figure 2. Porosity computation for invaded zone $R_{xo}$

## RESULT AND DISCUSSION

### Comparison with previous studies

To contextualize the present study within existing research, several analog and comparative investigations were reviewed. The Sleipner $CO_2$ storage project in the North Sea (Arts et al., 2004) provides an essential analog for supercritical $CO_2$–brine systems. Although the Sleipner study primarily used 4D seismic monitoring, it demonstrates how $CO_2$ injection alters the pore system connectivity and resistivity distribution, which conceptually aligns with the integration of density and resistivity logs employed in this work. In contrast, Suwondo et al. (2022) examined carbonate reservoirs in the Bintuni Basin (an analog to the Tangguh area) using log-based porosity estimation and found that dolomitic intervals exhibit overestimation when density logs are used alone—similar to the trends observed in this study.

Recent research by Kaczmarczyk-Kuszpit & Sowiżdżał (2024) on carbonate reservoirs in Poland integrated well logs and seismic attributes to improve porosity and lithofacies prediction, reinforcing the reliability of log integration for heterogeneous carbonate systems. Laboratory investigations by Hernández-Castro et al. (2019) also confirmed that $CO_2$-enriched brine can significantly modify porosity and resistivity responses in carbonates due to dissolution and mineral precipitation effects. These studies collectively support the methodology and findings of the present work, emphasizing that density–resistivity integration is an effective means of estimating porosity and distinguishing between connected and isolated pore systems in $CO_2$-water carbonate reservoirs.

### Porosity computation

Figure 3 shows the density log data used for quality control. The top section indicates a washout zone in soft limestone with high clay content, while the main reservoir interest lies in the Dolomite 1 interval. Despite rugosity effects, the density log signal depth of investigation (typically 15–20 inches) ensures that readings remain reliable. Mud cake buildup observed in the lower dolomite zone was assumed corrected using environmental corrections (spine-and-rib chart). Density corrections were within tolerance (<0.05), and gamma ray–density alignment confirmed that no additional depth shifting was necessary. These checks validate that the density log can be confidently applied in porosity computation.

Table 2. Summary of comparable studies and their relevance

| Study | Location/ lithology | Methodology | Key findings | Relevance to this study |
|---|---|---|---|---|
| Arts et al. (2004) | Utsira Formation, North Sea (sandstone aquifer) | 4D seismic $CO_2$ plume monitoring | Seismic anomalies trace $CO_2$ migration and pore connectivity evolution | Serves as an analog for $CO_2$–brine system behavior and pore connectivity context |
| Suwondo et al. (2022) | Carbonate (dolomite-limestone), Papua Barat | Log-based porosity (density-neutron) | Density log tends to overestimate porosity in dolomitic sections | Direct analog for carbonate lithology and log-based porosity overestimation |
| Kaczmarczyk-Kuszpit & Sowiżdżał (2024) | Carbonate platform, Poland | Integrated log-seismic inversion | Improved porosity estimation accuracy and heterogeneity mapping | Supports an integration approach for heterogeneous carbonate systems |
| Hernández-Castro et al. (2019) | Experimental carbonate core | $CO_2$-brine flow experiments | $CO_2$ alters porosity/ resistivity through dissolution and mineral precipitation | Confirms $CO_2$–brine influence on resistivity-porosity relations in carbonates |

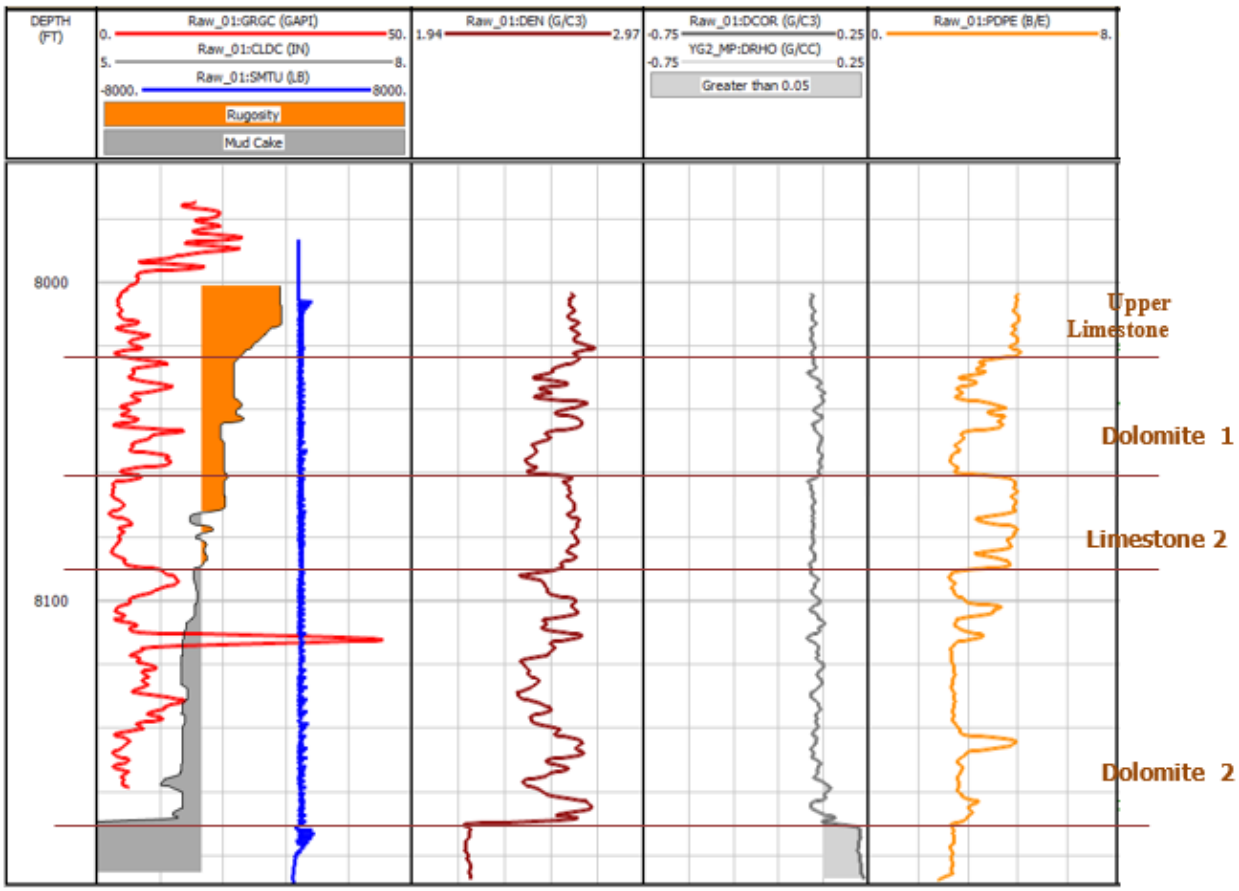


Figure 3. Density log data presented for quality control. The density track (left) shows washout effects in the upper limestone interval and more stable readings across the main reservoir sections. Lithology interpretation indicates four primary units: Upper Limestone, Dolomite 1, Limestone 2, and Dolomite 2. The rugosity log highlights zones affected by borehole enlargement, while the density correction curve displays intervals requiring caution during porosity estimation. These logs collectively confirm data reliability prior to density–resistivity integration.

### Neutron log assessment

The neutron log was recorded in limestone porosity units, using mnemonics NPRL and NPOR, which both produced consistent results. However, its application in porosity estimation was limited due to the presence of NaCl, which can distort hydrogen index readings. Furthermore, under supercritical $CO_2$ conditions, neutron counts do not correspond to hydrogen content, rendering the tool ineffective for estimating effective porosity. Thus, neutron logs were excluded from further analysis.

### Clay content estimation

Clay typing using the Schlumberger Lith-2 spectral gamma ray cross-plot (thorium vs. potassium) showed that the data did not cluster into any specific clay type (Figure 4). The absence of a pure shale zone implies that the clay influence on log responses is negligible. This justifies the exclusion of clay correction in subsequent porosity calculations.

### Core-log depth matching

To validate log interpretation, depth shifting was performed by aligning gamma ray and density logs with core measurements. Figure 5 shows good alignment after shifting, reducing mismatch, and enabling more reliable comparison between core and log-derived porosity. This calibration step is critical for ensuring the robustness of porosity interpretation.

### Supercritical $CO_2$ density validation

The supercritical $CO_2$ density was computed using Liang's correlation (2014) and compared with NIST data (Span & Wagner, 1996). As shown in Figure 6, the computation matched well at reservoir conditions (~3,602 psi, 132 °F) with an estimated density of 0.8056 g/cc. Slight overprediction at lower pressures (~3,000 psi) was observed relative to NIST data, while correlations from Wang et al. (2015) produced unrealistic values. This confirms the suitability of Liang's correlation for supercritical $CO_2$ density under field conditions.

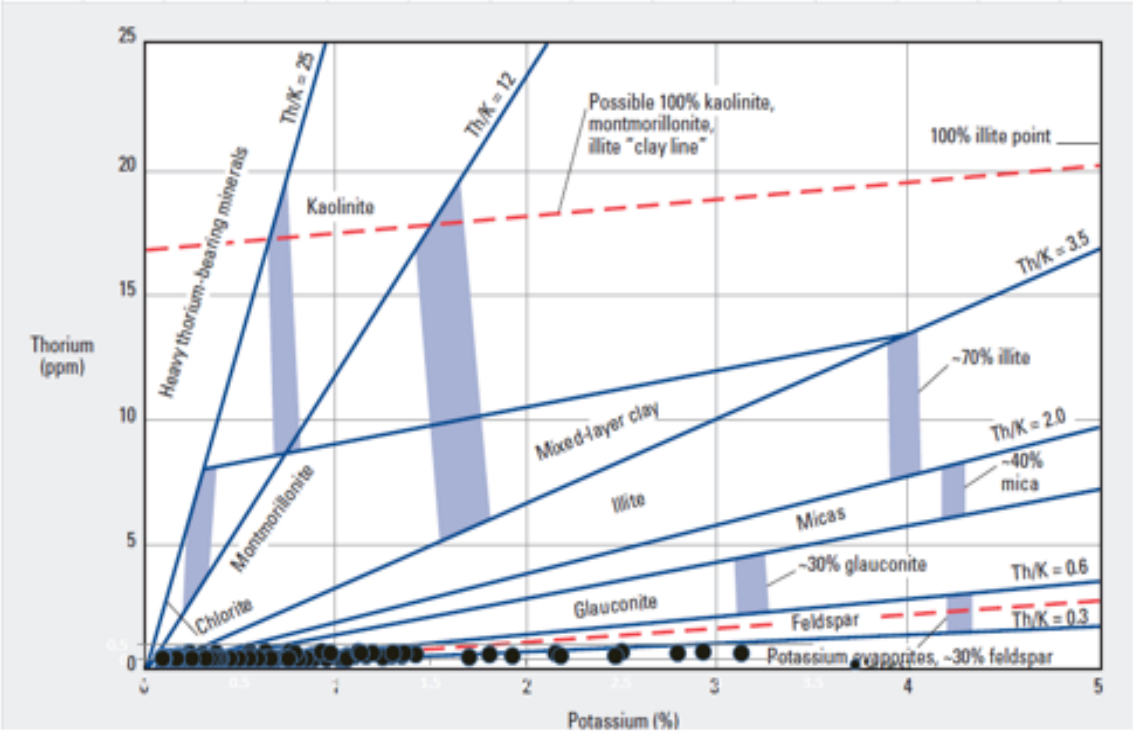


Figure 4. Figure 4. Clay mineral typing using spectral gamma ray crossplot of thorium versus potassium. The distribution of data points indicates the presence of mixed clay mineralogy, with zones trending toward kaolinite, illite, and chlorite fields. The Th/K trends also reveal intervals with higher heavy-mineral or mica content. This mineralogical classification supports the lithology interpretation and provides constraints on matrix density, neutron response, and porosity behavior in the carbonate reservoir units.

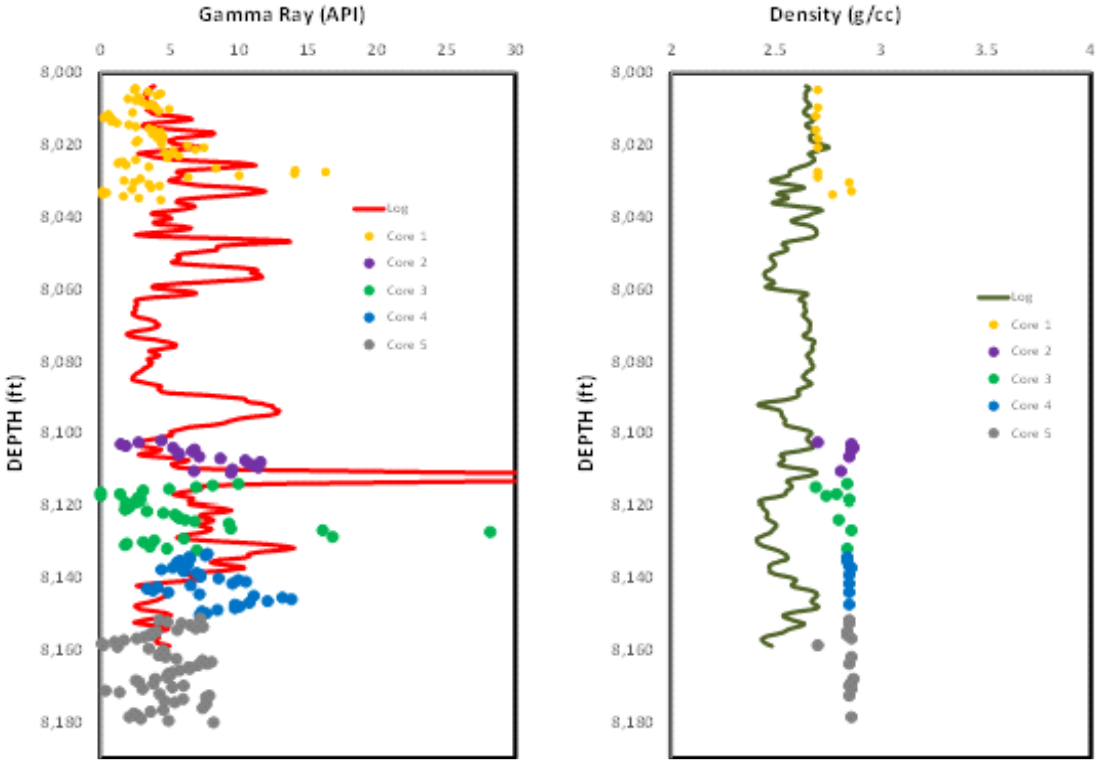


Figure 5. Core–log depth shifting for gamma ray and density measurements. The plotted core data from five core intervals are aligned against the corresponding well-log responses to correct depth mismatches caused by coring disturbances and depth-recording uncertainties. The alignment improves consistency between high-resolution core measurements and continuous log profiles, ensuring accurate calibration for porosity and lithology interpretation.

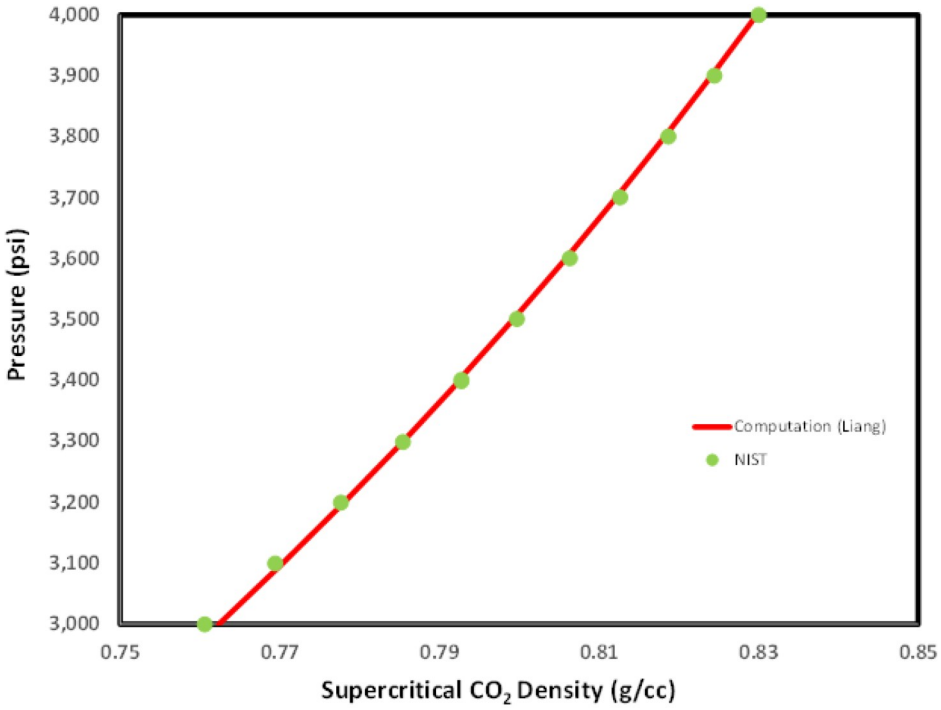


Figure 6. Comparison between computed supercritical $CO_2$ density (using Liang's correlation) and reference data from NIST. The strong agreement between the calculated curve and NIST measurements validates the reliability of the correlation across the reservoir pressure range (3,000–4,000 psi). This verification ensures that the $CO_2$ density used in the porosity computation is accurate for in-situ reservoir conditions.

### Mud invasion and resistivity response

Resistivity logs (R30O, R40O, R60O, R85O, RTAO) displayed separation between shallow and deep curves, confirming mud filtrate invasion (Figure 7). Deep resistivity readings are representative of the uninvaded zone, while shallow readings reflect invaded intervals. This observation necessitated separate porosity workflows for uninvaded (Rt) and invaded (Rxo) zones (Figures 1 and 2). Such differentiation ensures that porosity estimation accounts for invasion effects, which are common in carbonate reservoirs.

### Porosity estimation and core validation

Porosity was first estimated from density logs (total porosity) and then refined through integration with resistivity logs using Archie's equation (effective porosity). As shown in Figure 8 (left panel), density-only porosity consistently overestimated values in dolomitic zones by approximately 10%. The integrated approach provided more realistic estimates by excluding isolated, non-connected pores, underscoring the importance of incorporating resistivity in porosity analysis. Validation with core porosity measurements further confirmed the reliability of the integrated method. Figure 8 (right panel) shows that most dolomite intervals exhibit good agreement between core and log-derived porosity. Minor discrepancies were observed in low-porosity intervals (<5% at depths of 8,080–8,130 ft), which may require further verification. Overall, the integrated method demonstrated stronger correlation with core data compared to density log alone, reinforcing its robustness for porosity assessment in carbonate reservoirs.

### Isolated pore estimation

Carbonate reservoirs typically exhibit complex pore systems, including interparticle pores, vugs, and fractures. Diagenetic processes, such as dissolution and precipitation, strongly influence these heterogeneities. Dissolution caused by $CO_2$–brine–rock interactions can generate secondary porosity, enhancing the overall pore volume.

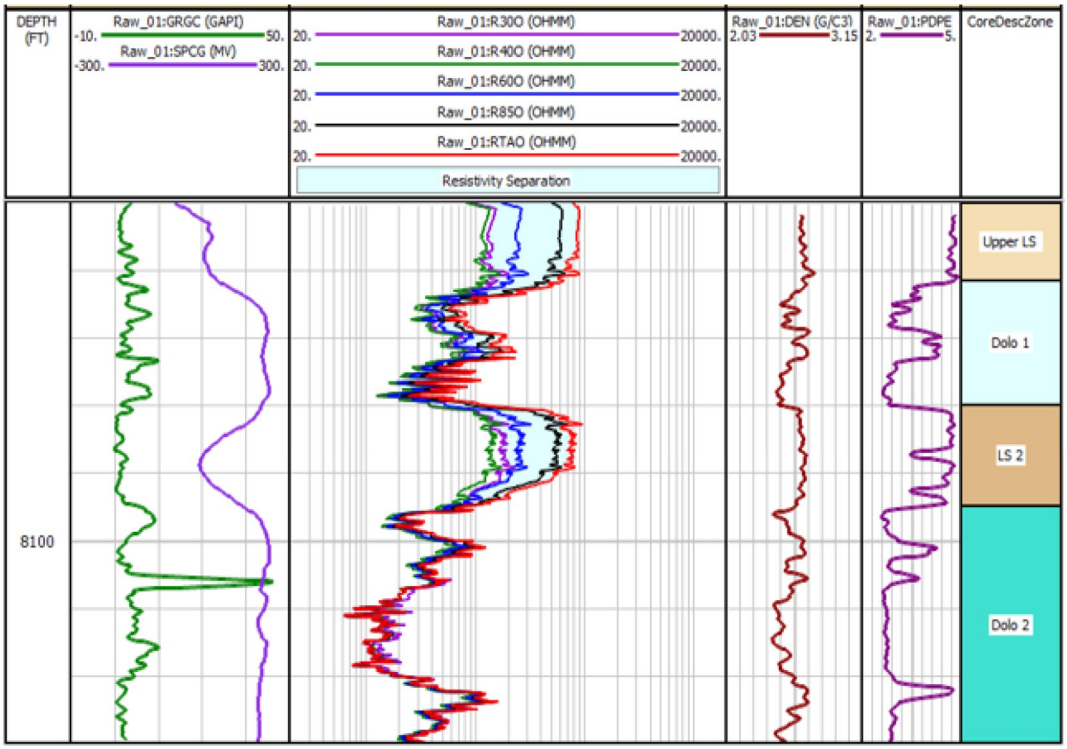


Figure 7. Resistivity log separation illustrating the extent of mud filtrate invasion across the carbonate intervals. The divergence between shallow, medium, and deep resistivity curves indicates zones where mud filtrate has displaced formation fluids, particularly within more porous intervals of the Upper Limestone, Dolomite 1, LS2, and Dolomite 2 units. This resistivity separation is critical for determining invaded-zone saturation (Sxo) and for ensuring accurate input to the integrated density–resistivity porosity calculation.

**Isolated pore estimation**

Carbonate reservoirs typically exhibit complex pore systems, including interparticle pores, vugs, and fractures. Diagenetic processes, such as dissolution and precipitation, strongly influence these heterogeneities. Dissolution caused by $CO_2$–brine–rock interactions can generate secondary porosity, enhancing the overall pore volume. Conversely, mineral precipitation (e.g., calcite or ankerite cementation) can occlude pore connectivity, leading to the development of isolated pores that are not hydraulically connected to the main flow system.

The comparison between core and log-derived porosity (Figure 9) highlights that while overall porosity trends are consistent, certain dolomitic intervals display discrepancies that may reflect the presence of isolated pores. These isolated pores were quantified as the difference between total porosity (derived from density logs) and effective porosity (derived from integrated resistivity–density analysis). As shown in Figure 10, the distribution of isolated pores is heterogeneously developed across the studied interval. The results indicate an average of approximately 2% isolated porosity in the upper dolomite and about 1.5% in the lower dolomite. Although these pores contribute to storage capacity by increasing total pore volume, they do not enhance fluid flow or permeability. Consequently, their presence may limit injectivity and reduce the efficiency of $CO_2$ storage operations.

From a CCS perspective, recognizing and quantifying isolated porosity is critical. While such pores can temporarily retain $CO_2$, they are unlikely to provide long-term benefits in terms of injectivity. Distinguishing between total and effective porosity, therefore, becomes essential in evaluating reservoir quality and ensuring realistic assessments of $CO_2$ storage performance in carbonate formations.

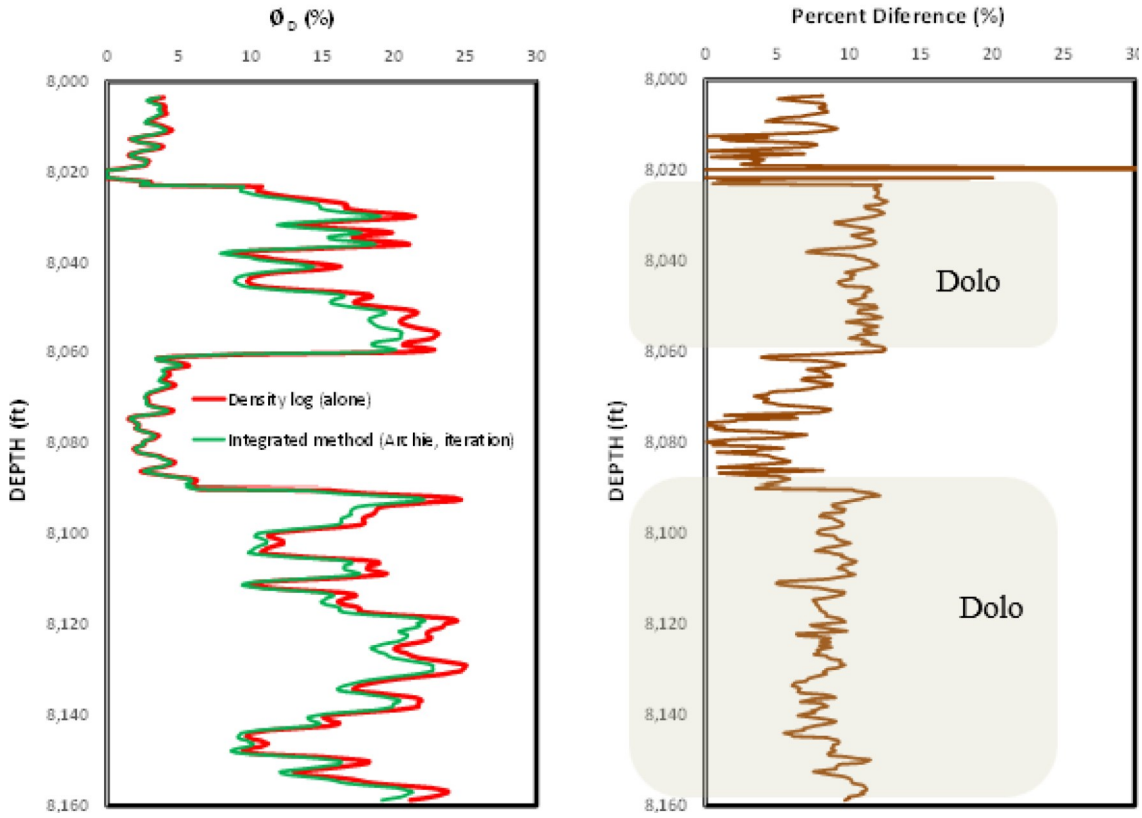


Figure 8. Comparison between porosity derived from density log alone and the integrated density–resistivity iterative method. The left track shows that the integrated method yields lower porosity estimates within dolomitic intervals, where density logs typically overestimate due to high matrix density and secondary porosity effects. The right track presents the percent difference, highlighting zones (shaded) where the integrated method significantly reduces overestimation. This comparison demonstrates the effectiveness of the integrated approach in improving porosity accuracy, particularly in heterogeneous dolomite layers.

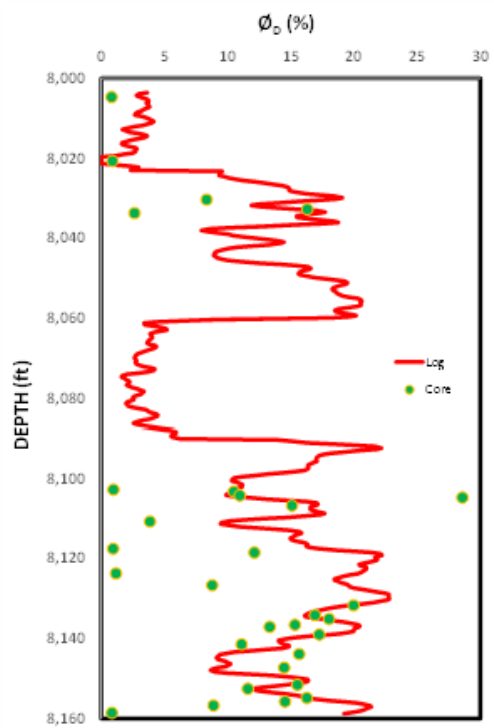


Figure 9. Comparison between log-derived porosity and core porosity measurements across the carbonate intervals. The log-derived porosity curve generally captures the overall porosity trend but shows noticeable deviations in dolomitic sections, where core measurements indicate lower porosity than suggested by logs. This comparison highlights the importance of calibration with core data and demonstrates the need for an integrated density–resistivity approach to reduce overestimation in heterogeneous carbonate reservoirs.

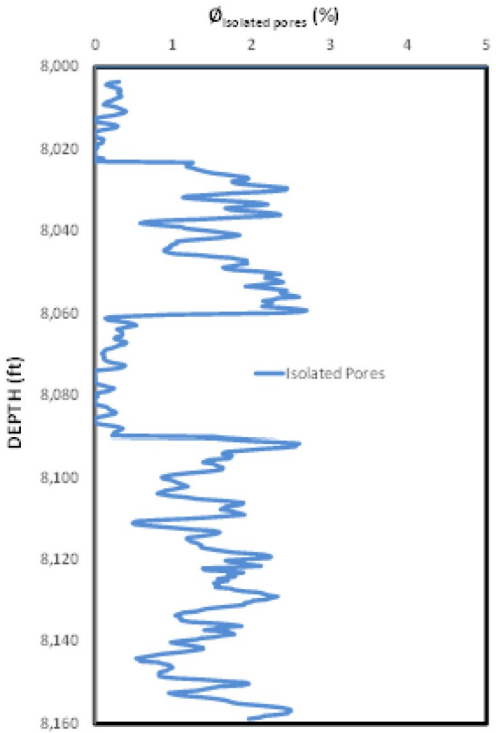


Figure 10. Estimated isolated□pore porosity across the carbonate intervals. The curve highlights depth zones where porosity occurs predominantly within unconnected or poorly connected pore spaces, which do not contribute to fluid flow. These isolated pores are typically associated with tight limestone layers and partially recrystallized dolomite intervals. Identifying isolated porosity helps differentiate effective porosity from total porosity and improves the reliability of reservoir quality assessment in CO□–water carbonate systems.

## CONCLUSION

This study emphasizes the significance of employing an integrated density–resistivity log approach for porosity estimation in natural carbonate $CO_2$ reservoirs. The results demonstrate that density logs alone tend to overestimate porosity, particularly in dolomitic zones, because they include both connected and isolated pores. By incorporating resistivity logs, it was possible to distinguish between total and effective porosity, leading to a more realistic representation of pore connectivity. Core validation further confirmed the robustness of this integrated method, showing closer agreement with measured porosity values compared to density-only estimations, with minor discrepancies observed in very low-porosity intervals.

Additionally, the study identified the presence of isolated porosity, averaging approximately 2% in the upper dolomite and 1.5% in the lower dolomite. While these isolated pores contribute to overall storage capacity, they do not improve permeability or injectivity, which are critical parameters for $CO_2$ storage performance. Recognizing and quantifying these differences is therefore essential in evaluating carbonate reservoirs for long-term geological storage.

Overall, the integrated workflow presented in this study provides a more accurate and comprehensive assessment of reservoir quality. By combining log data with fluid density computations and core validation, this approach enhances the reliability of porosity interpretation. It provides valuable insights for evaluating the suitability of natural $CO_2$ reservoirs as analogues for CCS and CCUS projects.

## ACKNOWLEDGEMENT

This work was financially supported by the Research, Community Service, and Innovation Program of the Faculty of Mining and Petroleum Engineering, Institute of Technology Bandung (ITB).

## GLOSSARY OF TERMS

| Symbol | Definition | Unit |
|---|---|---|
| $\rho$ | Density (general) | g/cc |
| $\rho b$ | Bulk density (log-derived) | g/cc |
| $\rho_{ma}$ | Matrix or grain density | g/cc |
| $\rho fa$ | Apparent fluid density (mixture of $CO_2$ and brine) | g/cc |
| $\rho w$ | Formation water (brine) density | g/cc |
| $\rho w@surface$ | Water density at surface conditions | g/cc |
| $\rho s_{co_2}$ | Supercritical $CO_2$ density | g/cc |
| $\rho_{mf}$ | Mud filtrate density | g/cc |
| $\rho e$ | Electron density | g/cc |
| $\rho a$ | Apparent density tool read- | g/cc |
| $\rho log\ reading$ | Density log recorded read- | g/cc |
| $\varphi$ | Porosity (general) | Fraction |
| $\varphi^{(0)}$ | Initial guess of porosity in iterative computation | Fraction |
| $\varphi D$ | Density-derived porosity | Fraction |
| $\varphi^{(n)}$ | Iterated porosity value in successive computation | Fraction |
| Rt | True formation resistivity (uninvaded zone) | ohm·m |
| Rxo | Shallow resistivity (invaded zone) | ohm·m |
| Rw | Formation water resistivity | ohm·m |
| $R_{mf}$ | Mud filtrate resistivity | ohm·m |
| Rmf@surface | Mud filtrate resistivity at the surface | ohm·m |
| Rmf@depth | Mud filtrate resistivity at depth | ohm·m |
| Sw | Water saturation | Fraction |
| Sxo | Water saturation in the invaded zone | Fraction |
| $Ss_{co_2}$ | Supercritical $CO_2$ saturation | Fraction |
| $Ss_{co_2a}$ | Supercritical $CO_2$ apparent saturation (Archie's con- | Fraction |
| a | Tortuosity factor (Archie's constant) | — |
| m | Cementation exponent | — |
| n | Saturation exponent | — |
| $A_0$–$A_4$ | Coefficients in Liang's $CO_2$ density correlation | — |
| $A_i$ | Polynomial coefficient dependent on temperature | — |
| $b_{i0}$–$b_{i4}$ | Polynomial constants used to calculate $A_i$ | — |

| | | |
|---|---|---|
| $B_W$ | Brine formation volume factor | bbl/STB |
| $\Delta V_{wT}$ | Temperature correction term for brine density | — |
| $\Delta V_{wp}$ | Pressure correction term for brine density | — |
| T | Temperature | °F |
| S | Salinity (total dissolved solids) | % |
| Z | Atomic number | — |
| MW | Molecular weight | g/mol |
| $NaCl_{ppm}$ | Salinity as sodium chloride equivalent | ppm |

## REFERENCES


Asquith, G. & Krygowski, D., (2004). Basic Well Log Analysis, AAPG Methods in Exploration Series, AAPG, Tulsa.

Arts, R., Eiken, O., Chadwick, A., Zweigel, P., van der Meer, L., & Zinszner, B., (2004). Monitoring of $CO_2$ injected at Sleipner using time-lapse seismic data. Energy, 29(9-10), 1383 –1392.

Bachu, S., (2008). $CO_2$ storage in geological media: role, means, status and barriers to deployment, Progress in Energy and Combustion Science, Vol. 34, No. 2, pp.254–273.

Doveton, J.H., (2014). Principles of Mathematical Petrophysics, Oxford University Press, Oxford.

ExxonMobil, 2024, The Outlook for Energy: A View to 2050, Exxon Mobil Corporation, Texas.

Gilfillan, S.M.V., Ballentine, C.J., Holland, G., Blagburn, D., Lollar, B.S., Stevens, S., Schoell, M. & Cassidy, M., (2009). The noble gas geochemistry of natural $CO_2$ gas reservoirs, Geochimica et Cosmochimica Acta, Vol. 72, No. 4, pp.1174–1198.

Hernández-Castro, D. M., Vidal Vargas, J. A., Koroishi, E. T., Lamas de Oliveira, L. F., & Trevisan, O. V., (2019). Porosity and Permeability Alteration of Carbonates by $CO_2$-Enriched Brine Injection. Materials Science Forum, 965, 107–115.

IEA, (2024). World Energy Outlook 2024, International Energy Agency, Paris.

IPCC, (2025.) Climate Change 2025: Synthesis Report, Intergovernmental Panel on Climate Change, Geneva.

Krevor, S., Blunt, M.J., Benson, S.M., Pentland, C.H., Reynolds, C., Al-Menhali, A. & Niu, B., (2015). Capillary trapping for geologic carbon dioxide storage, International Journal of Greenhouse Gas Control, Vol. 40, pp.221–237.

Kaczmarczyk-Kuszpit, E., & Sowiżdżał, A., 2024. Integration of Well Logging and Seismic Data for the Prognosis of Reservoir Properties of Carbonates. Energies, 17(2), 355.

Liang-Biao, O., (2014). New correlations for predicting the density and viscosity of supercritical carbon dioxide under conditions expected in carbon capture and sequestration operations, The Open Petroleum Engineering Journal, Vol. 4, pp.13–21.

Miocic, J.M., Gilfillan, S.M.V., Roberts, J.J., Edlmann, K., McDermott, C.I. & Haszeldine, R.S., (2013). Controls on $CO_2$ storage security in natural reservoirs and implications for $CO_2$ storage site selection, International Journal of Greenhouse Gas Control, Vol. 19, pp.19–30.

Rider, M. & Kennedy, M., (2011). The Geological Interpretation of Well Logs, Rider-French Consulting Ltd, Sutherland.

Span, R. & Wagner, W., (1996). A new equation of state for carbon dioxide covering the fluid region from the triple-point temperature to 1100 K at pressures up to 800 MPa, Journal of Physical and Chemical Reference Data, Vol. 25, No. 6, pp.1509–1596.

Suwondo, S., Utomo, W., Zera, T., & Almuqtadir, M. T., (2022). The analysis of Reservoir Porosity Calculation based on Well Log in Bintuni Basin Area. Journal of Natural Sciences and Mathematics Research, 8(1), 28–36.

Tiab, D. & Donaldson, E.C., (2015). Petrophysics: Theory and Practice of Measuring Reservoir Rock and Fluid Transport Properties, Gulf Professional Publishing, Oxford.

McCain, W.D., (1991). Reservoir-fluid property correlations – state of the art, SPE Reservoir Engineering, Vol. 6, No. 2, pp.266–272.

Wang, Z., Sun, B. & Tan, L., (2015). Improved density correlation for supercritical $CO_2$, Chemical Engineering & Technology, Vol. 38, No. 1, pp.75–84.